Applied Catalysis B: Environmental 289 (2021) 119783

Contents lists available at ScienceDirect

Applied Catalysis B: Environmental

journal homepage: www.elsevier.com/locate/apcatb

Boosting Pd-catalysis for electrochemical CO_2 reduction to CO on Bi-Pd single atom alloy nanodendrites

Huan Xie [a,b], Yangyang Wan [c], Xiaoming Wang [d], Jiashun Liang [a], Gang Lu [c], Tanyuan Wang [a], Guoliang Chai [b], Nadia Mohd Adli [e], Cameron Priest [e], Yunhui Huang [a], Gang Wu [e], Qing Li [a,*]

[a] State Key Laboratory of Material Processing and Die & Mould Technology, School of Materials Science and Engineering, Huazhong University of Science and Technology, Wuhan, Hubei, 430074, China
[b] State Key Laboratory of Structural Chemistry, Fujian Institute of Research on the Structure of Matter, Chinese Academy of Sciences, Fuzhou, 350002, Fujian, China
[c] Department of Physics and Astronomy, California State University - Northridge, Northridge, California, 91330, United States
[d] Department of Chemistry and Key Laboratory for Preparation and Application of Ordered Structural Materials of Guangdong Province, Shantou University, Shantou, 515063, China
[e] Department of Chemical and Biological Engineering, University at Buffalo, The State University of New York, Buffalo, NY, 14260, United States

ARTICLE INFO

Keywords:
Electrochemical CO_2 reduction
Single atom alloy
CO generation
Faradic efficiency
Electrocatalysis

ABSTRACT

Pd is a catalyst for electrochemical CO_2 reduction to CO but often disturbed by H_2 and formate formation at low overpotentials due to its strong affinity to H atoms. Herein, guided by density functional theory (DFT) calculations, Bi-Pd single atom alloy (SAA) nanodendrites (NDs) with Bi atomically dispersed in Pd matrices have been developed for efficient CO_2 reduction to CO. The Faradic efficiencies (FEs) of CO on the Bi_6Pd_{94}-SAA ND catalyst reach 90.5 % and 91.8 % in H-type and gas diffusion flow cells with overpotentials of only 290 and 200 mV, respectively, which are among the best of the reported Pd-based electrocatalysts. The greatly enhanced CO formation on the Bi_6Pd_{94}-SAA NDs can be attributed to the increased reaction barriers for H_2 formation due to a lower H coverage resulted from Bi doping, and the decreased free energy for *COOH generation which is a key intermediate for CO production.

1. Introduction

The large amount of anthropogenic CO_2 emission originated from the combustion of fossil fuels results in the dramatic increase of CO_2 concentration in atmosphere, which have triggered global concerns about the climate change and environmental degradations [1–5]. Electrochemical CO_2 reduction into value-added chemicals powered by renewable electricity sources (solar, wind, and geothermal energy, etc.) is one of the promising protocols to reach a carbon-balanced sustainable society [1,2,6–15]. CO is one of the main products by electrochemical CO_2 reduction reaction (CO_2RR), which finds wide uses in commercialized synthesis industries. Pure CO stream can be employed as the intermediate for the production of polycarbonate and polyurethane polymers [7]. Mixing CO with H_2, i.e., syngas, is the upstream material for the large-scale synthesis of bulk chemicals (methanol, acetic acid, and dimethyl ether, etc.) and synthetic fuels through well-established industrial processes [8,16–19].

CO_2RR to CO is a kinetically sluggish process with two electrons and protons transferred as indicated in the following reactions, which requires substantial overpotential [8,20,21] :

$$CO_2 + e^- + * \rightarrow *CO_2^- \quad (1)$$

$$*CO_2^- + H^+ \rightarrow *COOH \quad (2)$$

$$*COOH + H^+ + e^- \rightarrow CO + H_2O + * \quad (3)$$

where * denote the adsorption sites. Pd is among the well-known catalysts for CO formation via electrochemical CO_2RR due to its capability of generating and adsorbing *COOH, which is an essential intermediate for CO production [1–3,8,22–25]. However, due to the strong affinity of Pd to H atoms [26], the hydrogen evolution reaction (HER) is highly competitive with CO_2RR [19,27]. In addition, the formation of formate is preferred relative to CO at lower overpotentials (from 0 to -0.4 V) on Pd, due to a high degree of surficial H coverage [24,28,29]. These side reactions significantly lower the efficiency and selectivity of CO production. In order to solve these problems, the morphology [25,30,31],

* Corresponding author.
E-mail address: qing_li@hust.edu.cn (Q. Li).

https://doi.org/10.1016/j.apcatb.2020.119783
Received 23 July 2020; Received in revised form 18 November 2020; Accepted 23 November 2020
Available online 9 December 2020

exposing facets [32], size and supporting effects of Pd nanocrystals have been regulated [5,33]. Additionally, Pd has been alloyed with Cu [34,35], Au [36,37], Te [21], and Ag [5,38,39], in order to further tune the electronic and geometric structures of Pd [21]. With these efforts, the selectivity of CO_2RR to CO on Pd-based catalysts have been substantially improved (e.g., >90 %) but the required overpotential is still not satisfactory (typically between 390 mV and 790 mV, Table S1) [25,40].

Single atom alloy (SAA) metal catalysts have attracted considerable attention and demonstrated unique properties than the solute and host metals in electrocatalysis [41,42]. For instance, density functional theory (DFT) calculation screening of a series of SAA catalysts for electrochemical CO_2RR disclose that the cooperative catalysis between solute (Cu, Pd, Zn, and Co, etc) and host (Au, Ag) metals can lower the activation energy and tune the reaction pathways toward C1 hydrocarbon formation compared to monometallic counterparts [42,43]. Bi has much weaker adsorption of H atoms compared to Pd, and is capable of forming *COOH and generating a small part CO for CO_2RR [44,45]. In this work, density functional theory (DFT) calculations were first performed to simulate the free energy diagram of a Bi-Pd SAA catalyst for electrochemical CO_2RR. The results suggest that the introduction of single Bi atoms into Pd lattice is not only helpful to lower the H coverage on Bi-Pd surface against HER, but also can lower the formation free energy of *COOH intermediate, thereby facilitating highly selective CO formation. Guided by DFT calculations, Bi-Pd SAA nanodendrites (NDs) were successfully developed for efficient and selective electrochemical CO_2RR to CO. The Bi-Pd SAA NDs demonstrate the composition dependent CO_2RR performance, with Bi_6Pd_{94}-SAA revealing the highest Faraday efficiency (FE) and partial current density of CO formation. X-ray absorption spectroscopy (XAS) reveals that the coordination number (CN) of Bi-Bi bonds is quite lower than the bulk Bi, confirming the SAA nature of Bi-Pd NDs. The FEs of CO on the optimized C-Bi_6Pd_{94}-SAA ND catalyst reach 90.5 % and 91.8 % at -0.4 and -0.31 V vs. RHE in H-type cell and gas diffusion flow cell, respectively, with the overpotentials of only 290 and 200 mV, which is the lowest value among the reported Pd-based electrocatalysts for CO_2RR with FE_{CO} more than 90 %.

2. Experimental methods

2.1. Chemicals

Palladium acetylacetone ($Pd(ac)_2$, 99 %), bismuth neodecanoate (99 %), oleylamine (OA, 70 %), 1-octadecene (99 %) and 1-dodecanethiol (99 %) were purchased from Sigma-Aldrich. Ascorbic acid (AA, 99 %), n-hexane (99 %), isopropanol (99 %), methanol (99 %), ethanol (99 %), n-Butylamine (99 %), poly-vinylidenefluoride (PVDF, 99 %), n-methyl-2-pyrrolidone (NMP, 99 %), and potassium bicarbonate (99 %) were provided by Sinopharm Chemical Reagent Corporation. Carbon paper (TGP-H-60) was bought from Toray Corporation. All chemicals were used as received without further purifications.

2.2. Synthesis of Pd and Bi-Pd SAA NDs

For the synthesis of Pd NDs, 36.6 mg $Pd(ac)_2$ and 100 mg AA were dissolved in 5 mL OA. The solution was transferred into a 100 mL four-neck flask and heated to 120 °C with a ramping rate of 10 °C/min and maintained for 1 h under Ar atmosphere. After cooling down to room temperature, the NDs were washed and centrifuged (9000 r/min) with ethanol several times. The collected NDs were dispersed in n-hexane for further use. Bi-Pd SAA NDs were synthesized with the same processes and certain amounts of bismuth neodecanoate (5, 10 and 20 μL) were added into the original solution. Inductively coupled plasma mass spectroscopy (ICP-MS) tests indicated that the Bi to Pd ratios in Bi-Pd SAA nanodendrites were Bi_3Pd_{97}, Bi_6Pd_{94} and $Bi_{11}Pd_{89}$, respectively.

2.3. Synthesis of Bi nanoparticles (NPs)

630 μL bismuth neodecanoate and 5 mL 1-octadecene in 100 mL four-neck flask was heated at 80 °C for 30 min under Ar atmosphere. Then 10 mL 1-dodecanethiol was injected into to form a lightly yellow solution. After 30 min, 10 mL OA was injected quickly into the former solution and maintained at 80 °C for 20 min. After cooling down, the NPs were centrifuged and washed with a mixture of methanol and ethanol (volume ratio 1:4) several times. The resulted Bi NPs were dispersed in n-hexane.

2.4. Preparation of working electrodes

Pd and Bi-Pd SAA NDs, as well as Bi NPs were deposited on carbon black support for CO_2RR test. Briefly, 20 mg carbon black (Ketjen EC-300 J) was ultrasonically dispersed in the solution containing isopropanol and n-hexane (volume ratio 1:2). 20 mg the obtained Pd, Bi-Pd SAA NDs, and Bi NPs (capped with surfactants) suspended in n-hexane were dropwise added into the mixture and sonicated for 1 h. The catalysts were collected by centrifugation (9000 r/min). In order to remove the surfactants on NDs, they were dispersed in 50 mL n-butylamine and stirred under ambient conditions for 24 h. The catalysts were washed and centrifuged with ethanol several times, and dried in a vacuum oven at 60 °C for overnight. The mass loading amounts of Pd and Bi atoms on carbon for C-Bi_3Pd_{97}-SAA, C-Bi_6Pd_{94}-SAA and C-$Bi_{11}Pd_{89}$-SAA ND catalysts were 24 %, 25 %, and 28 %, respectively, which were measured by ICP-MS tests. For the preparation of working electrode, 2 mg PVDF, 3 mg catalysts, and several drops of NMP were mixed. The mixtures were painted onto both sides of the carbon paper (with size of 1.0 cm × 1.0 cm), and then dried in a vacuum oven at 60 °C for overnight.

2.5. Electrochemical CO_2 reduction tests in an H-type cell

Electrochemical CO_2RR tests were performed in a gas-tight H-type cell with a total volume of 30 mL combined with an electrochemical workstation (CHI760e, Chenhua). The anodic and cathodic chambers were separated by a proton exchange membrane (Nafion®212, Dupont). An Ag/AgCl electrode (4.0 M KCl) and 99.9 % platinum gauze were used as the reference and counter electrodes. The CO_2-saturated 0.5 M $KHCO_3$ solution was used as the electrolyte (PH = 7.3). The flow rate of CO_2 during CO_2RR test was maintained at 20 mL/min. All tested potentials were converted to the reversible hydrogen electrode (RHE) scale by measuring the potential difference between Ag/AgCl electrode and RHE.

Gaseous products were directed into the sample loop of a gas chromatograph (Shimadzu GC-2014) for composition analysis. Liquid products were collected after electrolysis and characterized by a ^1H nuclear magnetic resonance (NMR) spectrometer (Bruker AscendTM 600 MHz). For NMR test, 0.5 mL electrolyte, 0.15 mL D_2O and 0.1 mL DMSO aqueous solution (with a concentration of 0.5 μL/mL and used as internal standard) were mixed. The faradic efficiencies (FEs) of gaseous and liquid products were calculated as previous reports [8,10].

2.6. Electrochemical CO_2 reduction tests in a gas diffusion flow cell

Electrochemical CO_2RR tests were performed in a gas diffusion flow cell consisting of a gas-diffusion layer (CeTech W1S1009) deposited with C-Bi_6Pd_{94}-SAA (1.56 mg/cm^2) as the working electrode, nickel foam (1 mm) as the counter electrode, and Ag/AgCl (4.0 M KCl) as the reference electrode, and they are separated with polyether-ether-ketone (PEEK) spacers. The anion exchange membrane (AMI-7001) was used to separate the anodic and cathodic chambers. Ar-saturated 1.0 M KOH solution was used as the electrolyte. The flow rates of CO_2 and electrolyte were maintained at 10 and 40 mL/min during electrolysis, respectively. Other configurations were the same to that in an H-type cell. The reported potentials were iR-compensated by extracting the potential loss between the working and counter electrodes.

2.7. Characterizations

Transmission electron microscopy (TEM) and high-resolution TEM (HRTEM) images were taken from FEI Tecnai G2 F30 microscopies operated at 200 kV. X-ray diffraction (XRD) patterns were collected with a powder diffractometer (Rigaku Miniflex600) using Cu Kα radiation. High angle annular dark field-scanning transmission electron microscopy (HAADF-STEM) images and energy dispersive spectroscopy (EDS) elemental mapping images were obtained by a Thermo Fisher Talos F200X TEM operated at 200 kV. Surficial Bi to Pd ratios and their valence states were characterized by X-ray photoelectron spectroscopy (XPS, Shimadzu-Kratos XIS-ULTRA DLD-600W) using Mg Kα X-ray source. The binding energies of collected data were calibrated by referencing C 1s binding energy (284.6 eV). X-ray absorption spectroscopy (XAS) including X-ray absorption near edge spectroscopy (XANES) and extended X-ray absorption fine structure (EXAFS) of Bi L_3-edge and Pd K-edge were measured by Taiwan BL-12B2 Beam Line at SPring-8. The electron-storage ring was operated at 8 GeV with a constant current of 100 mA. A Si (111) double-crystal monochromator was used for the energy selection with resolution dE/E better than 2×10^{-4} at elemental edges. All XANES spectra of Bi L_3-edge and Pd K-edge were recorded at room temperature in fluorescence mode.

2.8. DFT calculations

The theoretical calculations were performed using Vienna Ab initio Simulation Package (VASP) [46,47] with projector augment wave (PAW) [48,49] method and GGA-RPBE [50–52] functional. The Pd (111) and Bi (001) surfaces were modeled by 4-atomic-layer slabs with 15Å vacuum. The energy cutoff for the planewave bases was 400 eV and the positions of surface atoms were optimized with convergence criteria of 10^{-5} eV and 0.01 eV/Å for energy and force, respectively. The cutoff energy of 400 eV was used for both optimization and self-consistent calculation. The Brillouin zones are were sampled with $6 \times 6 \times 1$ and $6 \times 4 \times 1$ Gamma-centered k-points for Pd(111) and Bi(001), respectively. DFT-D3 [53] method was used to describe the dispersion correction and the solvation effect of water was described by an implicit solvation model [54]. Computational hydrogen electrode (CHE) model [55,56] was used to calculate the free energy change of hydrogen evolution and CO_2 reduction reactions. The free energy was calculated with the equation: $G(T) = E + H(T) - TS(T)$, where E denoted the energy in self-consistent calculation, and $H(T)$ and $TS(T)$ are enthalpy and entropy at a given temperature. Here, the temperature of 298 K was used. For gas molecules, the contribution of enthalpy and entropy of vibration, rotation, and translation were considered; while for adsorbed species, only the contribution of vibration was considered because the rotation and translation were limited. The free energy of one proton and one electron ($G(H^+ + e^-)$) was replaced with $1/2G(H_2)$, considering that the reaction of $H^+ + e^- = 1/2H_2$ was in equilibrium state at standard condition. Note that the free energy is calculated in the absence of an applied electric field, thus our theoretical model cannot capture the field or potential-dependence of catalytic activity. In all calculations, adsorbates and the first two layers were relaxed, while the other atoms were fixed to the optimized bulk positions. The Bi-Pd SAA system was modeled by replacing one Pd atom with one Bi atom in the 4 layer Pd(111) surface, with the Bi atomic ratio of 6.25 % (denoted as Bi_1Pd_{15}). According to the calculated energies of Bi_1Pd_{15} with Bi atom in the first and second layer, we find that Bi prefers to occupy the first layer of Pd(111) surface, as shown in Fig. S1. Considering that the adsorption of H leads to H-covered Pd surfaces under the CO_2 reduction condition [29], the H-covered Pd(111) and BiPd(111) surface were used to calculated the free energy change of HER and CO_2 reduction.

3. Results and discussion

3.1. DFT calculations for CO_2RR on Pd, Bi, and Bi-Pd SAA surfaces

It is known that the most stable H coverage on pure Pd surface is one monolayer (1 ML), owing to the strong affinity of H on Pd surface during electrolysis [21,29]. The higher coverage of H on the Pd surface should promote formate formation at the potential from 0 to -0.2 V vs. reversible hydrogen electrode (RHE), and H_2 formation from -0.3 to -0.4 V vs. RHE [29]. However, we find that the optimal H coverage on Bi_1Pd_{15}(111)-SAA is 1/2 ML (Figs. 1 and S2), indicating that Bi on the Pd surface tends to lower H coverage. In addition, the thermodynamic energy barrier of HER increases accordingly from 0.72, 0.89, to 1.22 eV on Pd(111), Bi_1Pd_{15}(111)-SAA, and Bi(001) (Fig. 1), respectively. The higher thermodynamic energy barrier of HER on Bi_1Pd_{15}(111)-SAA compared to Pd suggests that the reduced H coverage would impede H_2 formation on Bi_1Pd_{15}(111)-SAA during CO_2RR. Moreover, the free energy for *COOH formation on Bi_1Pd_{15}(111)-SAA (1.2 eV) is reduced by 0.3 eV as compared to that on Pd(111) surface (1.5 eV) (Fig. 1). Since *COOH is the key intermediate for CO formation, we predict that the overpotential for CO formation on Bi_1Pd_{15}(111)-SAA is lower than that on Pd(111) surface. In other words, DFT calculations suggest that Bi-Pd SAA with an appropriate amount of Bi could reduce the overpotential for CO formation and simultaneously suppress the competing H_2 formation.

3.2. Synthesis and structural characterizations of Bi-Pd SAA NDs

Guided by DFT calculations, in this work Bi-Pd SAA NDs with different Bi contents, i.e., Bi_3Pd_{97}, Bi_6Pd_{94} and $Bi_{11}Pd_{89}$, were synthesized by reducing palladium acetylacetone ($Pd(ac)_2$) and bismuth neodecanoate using acetic acid (AA) as the reducing and morphology regulating agent in oleylamine (OA) solution (illustrated in Fig. 2a). The unique ND morphology originates from the regulated crystal growth of Pd by AA, which renders a larger surface area and more exposed active facets for catalysis [38,57]. TEM and HAADF-STEM images of Pd and three Bi-Pd SAA catalysts (Fig. 2b–e, Fig. S3, and Fig. 3a, d, g) demonstrate the ND morphologies. The size of Pd NDs is ~20−30 nm (Fig. 2b–c), and the sizes of Bi_3Pd_{97}-SAA, Bi_6Pd_{94}-SAA and $Bi_{11}Pd_{89}$-SAA NDs are slightly reduced to ~10−15 nm (Figs. 2d–e and S3), likely due to the hampered crystal growth of NDs after introducing Bi. HRTEM images of Pd, Bi_3Pd_{97}-SAA, Bi_6Pd_{94}-SAA, and $Bi_{11}Pd_{89}$-SAA NDs (Figs. 2f–g and S3) indicate that the lattice spacings of (111) facets of Bi-Pd NDs are apparently increased compared to pure Pd due to a larger atomic size of Bi (0.147 nm) than Pd (0.128 nm). Moreover, from the EDS elemental mapping images of Bi-Pd SAA NDs (Fig. 3), it can be clearly seen that Bi is incorporated into Pd lattice and distributed evenly. For further electrochemical tests, these NDs are dispersed on carbon support (denoted as C-Pd and C-Bi-Pd SAA) without apparent agglomerations (Fig. S4). Additionally, Bi NPs (~80 nm) are also prepared and dispersed on carbon support as a control sample (C-Bi, Fig. S5).

The XRD patterns of C-Pd and C-Bi catalysts (Figs. 4a and S6) match well with the peaks of Pd (cubic, JCPDS# 05-0681) and Bi (rhombohedral, JCPDS# 44-1246). The diffraction patterns of C-Bi_3Pd_{97}-SAA, C-Bi_6Pd_{94}-SAA and C-$Bi_{11}Pd_{89}$-SAA catalysts resemble to that of C-Pd (Fig. 4a), but all of the peak positions are left shifted relative to C-Pd, indicating that Bi atoms are incorporated into Pd lattice increasing their lattice spaces due to the larger atomic size of Bi. Notably, the peak positions of C-Bi_6Pd_{94}-SAA and C-$Bi_{11}Pd_{89}$-SAA are comparable, likely due to the fact that Bi atoms in C-$Bi_{11}Pd_{89}$-SAA are more concentrated on the surface rather than in the bulk crystal structure, as evidenced by ICP-MS and XPS measurements (Table S2).

The XPS survey spectra of these catalysts (Fig. S7) indicate that only Bi, Pd, C, and O elements are detected. The high-resolution XPS spectra of Pd 3d electrons of C-Pd, C-Bi_3Pd_{97}-SAA, C-Bi_6Pd_{94}-SAA, and C-$Bi_{11}Pd_{89}$-SAA ND catalysts (Fig. 4b) indicate that both metallic Pd (the binding energies of $3d_{3/2}$ and $3d_{5/2}$ electrons are 340.9 and 335.6 eV,

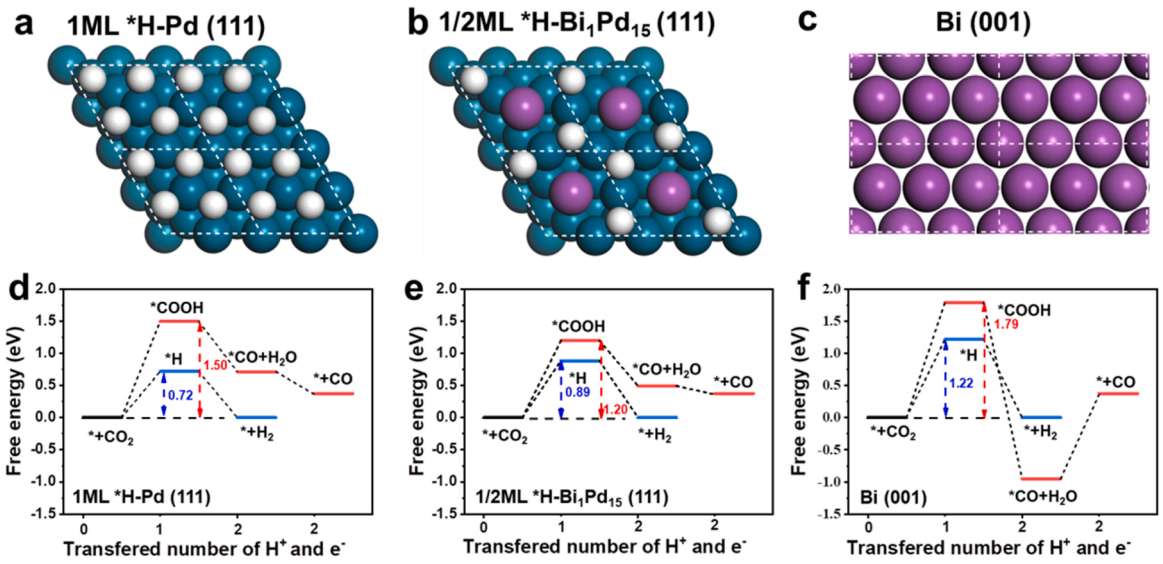

Fig. 1. Optimized geometries of (a) Pd(111), (b) Bi_1Pd_{15}(111)-SAA and (c) Bi(001) systems, in which Pd(111) is covered with 1 monolayer (ML) of H and Bi_1Pd_{15}(111)-SAA system is covered with 1/2 ML of H, and the blue, purple and white balls denote Pd, Bi and H atoms, respectively. The free energy changes of HER and CO formation for CO_2RR on (d) Pd(111), (e) Bi_1Pd_{15}(111)-SAA and (f) Bi(001) surfaces, * denotes the pristine surface.

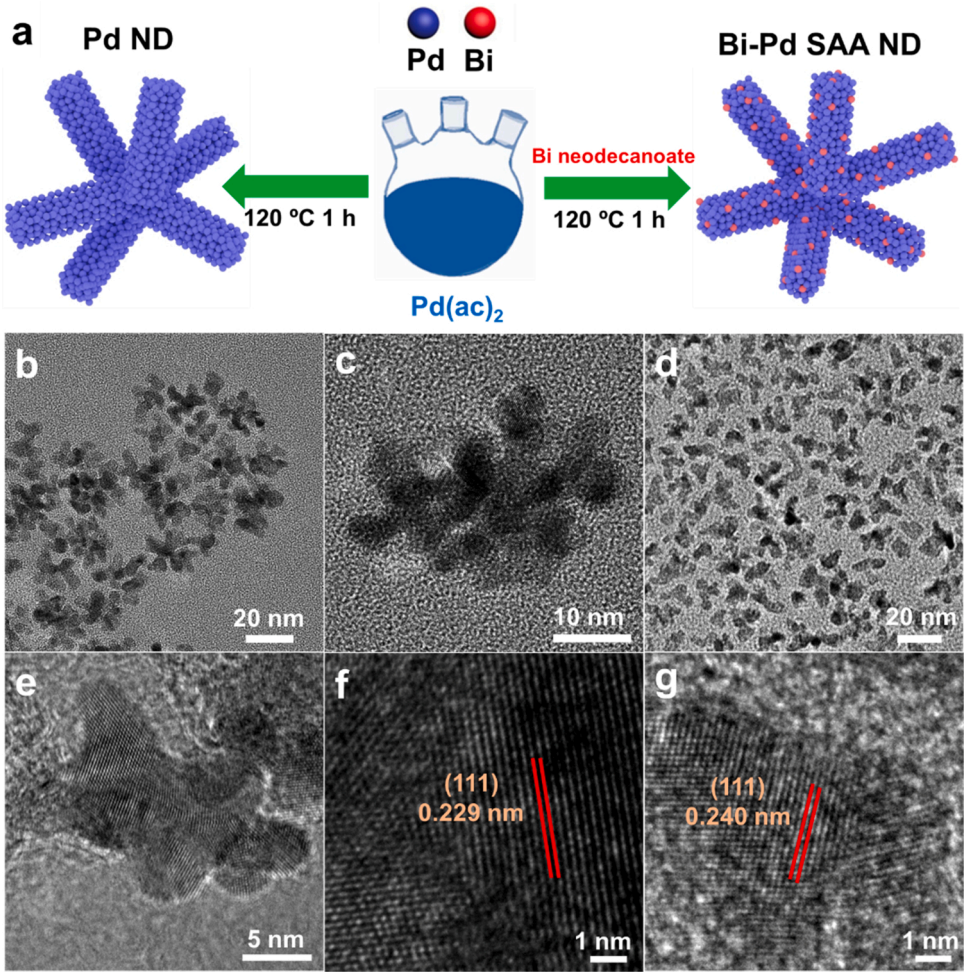

Fig. 2. (a) Schematic illustration of the synthetic processes of Pd and Bi-Pd SAA NDs. TEM images of (b-c) Pd and (d-e) Bi_6Pd_{94}-SAA NDs. HRTEM images of (f) Pd and (g) Bi_6Pd_{94}-SAA NDs.

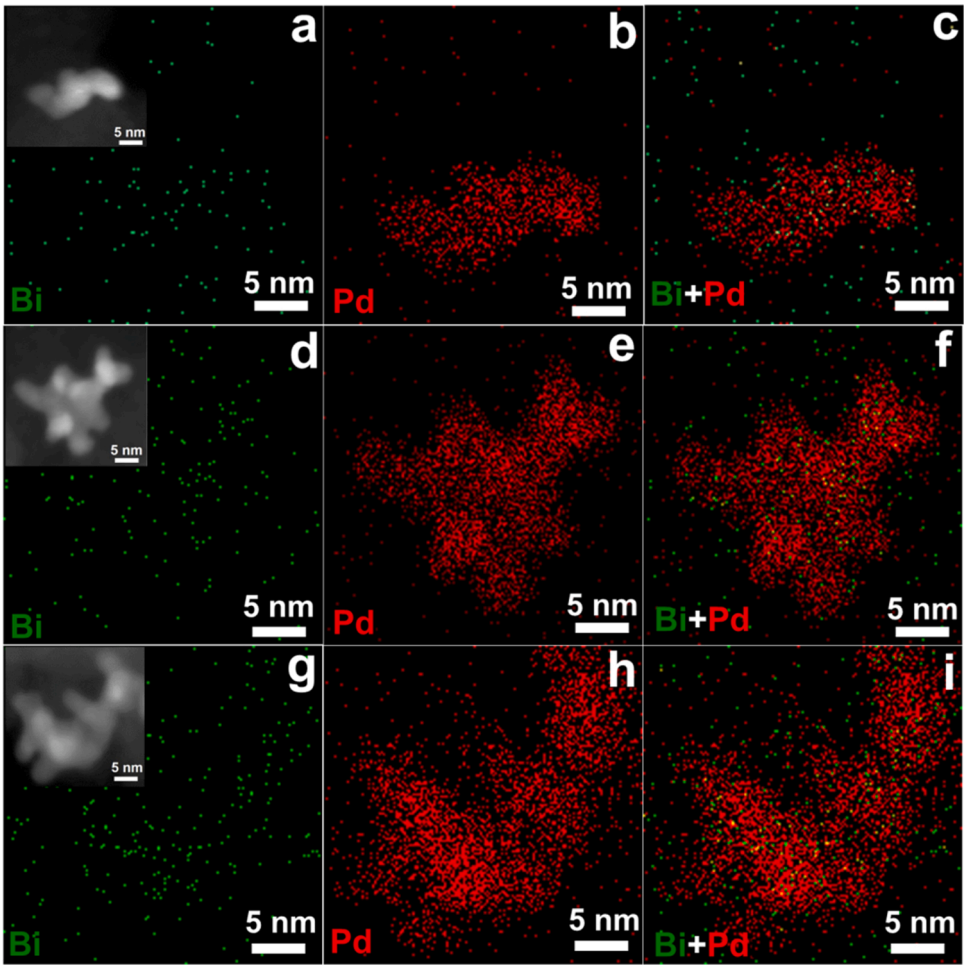

Fig. 3. EDS elemental mapping images of Bi (green) and Pd (red) of (a-c) Bi_3Pd_{97}-SAA, (d-f) Bi_6Pd_{94}-SAA, and (g-i) $Bi_{11}Pd_{89}$-SAA NDs, the insets in (a), (d), and (g) are the HAADF-STEM images.

respectively) and a small portion of Pd^{2+} (the binding energies of $3d_{3/2}$ and $3d_{5/2}$ electrons are 342.0 and 336.5 eV, respectively) exist due to slight surficial oxidation after exposure in air [21,37]. In addition, the binding energies of Pd in C-Bi_3Pd_{97}-SAA and C-Bi_6Pd_{94}-SAA ND catalysts are shifted to the lower direction compared to pure C-Pd, which may be attributed to the electrons transfer from Bi to Pd due to the smaller work function of Bi (4.31 eV) than Pd (5.22 eV). In contrast, the binding energy of Pd in C-$Bi_{11}Pd_{89}$-SAA is shifted to higher direction in comparison to C-Pd, C-Bi_3Pd_{97}-SAA, and C-Bi_6Pd_{94}-SAA catalysts. Besides, the high-resolution Bi 4f XPS spectra of C-Bi_3Pd_{97} and C-Bi_6Pd_{94} catalysts (Fig. S8) reveal that only metallic Bi can be detected, with binding energies of 162.8 eV ($4f_{5/2}$ peak) and 157.2 eV ($4f_{7/2}$ peak). For C-$Bi_{11}Pd_{89}$-SAA, a small portion of Bi^{3+} (164.8 and 159.3 eV for $4f_{5/2}$ and $4f_{7/2}$ electrons, respectively) also exists in parallel to metallic Bi [44, 58]. Similar to Pd, the binding energies of Bi-related peaks in C-$Bi_{11}Pd_{89}$-SAA left shift compared to C-Bi_3Pd_{97}-SAA and C-Bi_6Pd_{94}--SAA, which probably originates from the existence of Bi^{3+} and the concentrated Bi atoms on the surface of C-$Bi_{11}Pd_{89}$-SAA, resulting in the different electronic structure of C-$Bi_{11}Pd_{89}$-SAA catalyst. The Bi 4f XPS spectra of C-Bi catalyst (Fig. S8) is dominated by Bi^{3+} and only a limited portion of metallic Bi can be detected due to the surficial oxidation of Bi NP. These results illustrate that doping Bi in Pd lattice is helpful to prevent the oxidation of Bi, which can be ascribed to the charge transfer between Bi and Pd atoms. In addition, C-$Bi_{11}Pd_{89}$-SAA demonstrates higher surficial Bi/Pd (0.05) and surficial/total Bi (0.45) ratios than that of C-Bi_3Pd_{97}-SAA (0.01 and 0.33) and C-Bi_6Pd_{94}-SAA (0.02 and 0.33) (Table S2), inferring that Bi atoms in the C-$Bi_{11}Pd_{89}$-SAA catalyst are prone to appear on the surface due to the limited solubility of Bi in Pd lattice.

To explore the valence states and local coordination structures of Bi-Pd SAA NDs, X-ray absorption spectroscopy (XAS) including X-ray absorption near edge structure (XANES) and extended X-ray absorption fine structure (EXAFS) spectra were performed (Fig. 4c–f). The adsorption edge of XANES spectra of Pd K-edge and Bi L_3-edge (Fig. 4c, e) for C-Bi_3Pd_{97}-SAA, C-Bi_6Pd_{94}-SAA, and C-$Bi_{11}Pd_{89}$-SAA NDs are similar and close to the reported spectra of standard Pd and Bi foils [35,59], indicating that Pd and Bi mainly exist as the metallic form in the developed Bi-Pd SAA NDs. The k^3-weighted FT-EXAFS spectra of the studied catalysts are fitted (Fig. S9) and the results are summarized in Table S3. For Pd K-edge k^3-weighted FT-EXAFS spectra (Fig. 4d), the main peaks at 2.54 and 1.56 Å corresponds to Pd-Pd and Pd-O bond, respectively [35]. With the increase of Bi amount in Bi-Pd SAA catalysts, the bond length of Pd-Bi is slightly reduced (Table S3) and the coordination number (CN) of Pd-Bi (0.509, 1.172, and 1.526) is increased, indicating that the Bi-Pd SAA catalysts remains the crystal structure of Pd as indicated by the XRD patterns (Fig. 4a). In Bi L_3-edge k^3-weighted FT-EXAFS spectra (Fig. 4f), the peaks at 2.56 and 1.73 Å can be ascribed to the Bi-Pd and Bi-O coordination shells, respectively [60]. With the increase of Bi amount, the bond length and CN (9.959, 8.431, and 7.318) of Bi-Pd are both slightly decreased (Table S3). Theoretically, if Bi is incorporated into Pd lattice, more Bi-Pd bonds would be formed, and the bond length of Bi-Pd should raise with the increase of Bi amount, meanwhile the CN of Bi-Pd should remain unchanged. The results further testify that with the increase of Bi content in Bi-Pd SAA ND catalysts, Bi tends to

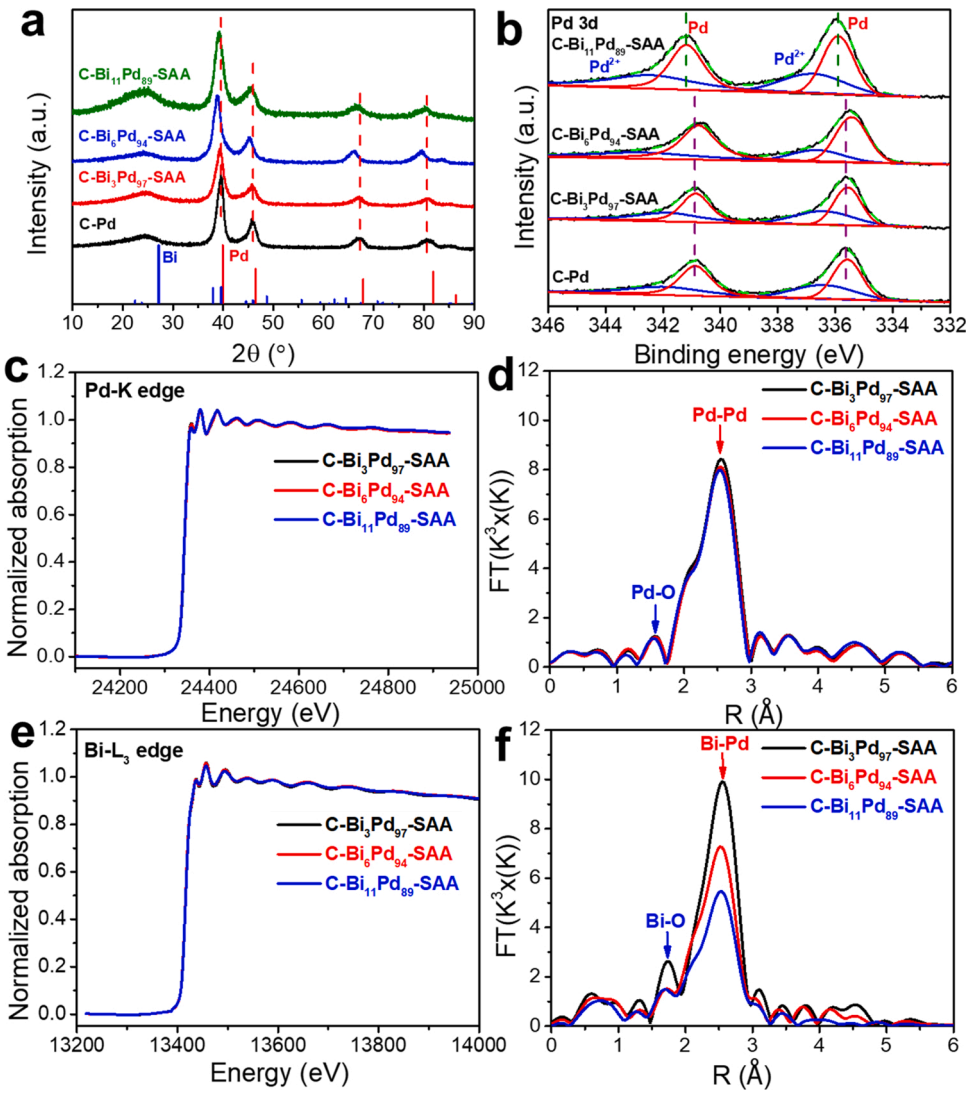

Fig. 4. (a) XRD patterns and (b) high-resolution XPS spectra of Pd 3d electrons of C-Pd and C-Bi-Pd SAA ND catalysts. Pd K-edge (c) XANES and (d) k^3-weighted FT-EXAFS spectra of C-Bi-Pd SAA ND catalysts. Bi L_3-edge (e) XANES and (f) k^3-weighted FT-EXAFS spectra of C-Bi-Pd SAA ND catalysts.

concentrate on the surface rather than in the lattice as has been demonstrated by the combination of XPS and ICP-MS tests (Table S2). Additionally, the CNs of Bi-Bi bonds in C-Bi_3Pd_{97}-SAA, C-Bi_6Pd_{94}-SAA, and C-$Bi_{11}Pd_{89}$-SAA are 0.472, 0.902, and 1.126 (Table S3), respectively, which are significantly lower than that of bulk Bi (CN = 12) [39]. Obviously, no Bi-Bi bond (2.90 Å) is observable in the k^3-weighted FT-EXAFS spectra of C-Bi-Pd SAA ND catalysts (Fig. 4f), indicating that Bi atoms are atomically dispersed in the developed Bi-Pd SAA catalysts.

3.3. Electrochemical study for Bi-Pd SAA ND catalysts

The performance of C-Pd, C-Bi-Pd SAA NDs, and C-Bi catalysts for electrochemical CO_2RR were first evaluated in an H-type cell. The linear sweep voltammetry (LSV) curves of C-Pd, C-Bi_3Pd_{97}-SAA, and C-Bi_6Pd_{94}-SAA ND catalysts in CO_2-saturated 0.5 M $KHCO_3$ solution resemble to each other (Fig. 5a), while the C-$Bi_{11}Pd_{89}$-SAA ND catalyst demonstrates greatly enhanced current density from 0 to -1.0 V vs. RHE. The cyclic voltammetry (CV) curves of these catalysts in CO_2-saturated 0.5 M $KHCO_3$ solution (Fig. 5b) indicate that the C-Bi_6Pd_{94}-SAA ND catalyst has much weaker peaks of H adsorption (0.14 V) and H desorption (0.12 and 0.46 V) compared to other catalysts, demonstrating the weakened H affinity on C-Bi_6Pd_{94}-SAA NDs. Besides, the C-$Bi_{11}Pd_{89}$-SAA NDs show the strongest H affinity among the Bi-Pd SAA ND catalysts, which is comparable to that of C-Pd catalyst. The large current densities observed on C-$Bi_{11}Pd_{89}$-SAA and C-Pd ND catalysts can be ascribed to the strongly competitive HER during CO_2RR.

The FEs of various products for electrochemical CO_2RR on C-Pd, C-Bi-Pd SAA NDs and C-Bi catalysts at different potentials in H-type cell are calculated and illustrated in Fig. 5c–d and Fig. S10. For the pristine C-Pd ND catalyst, the electrochemical CO_2RR produces CO (Fig. 5c), H_2 (Fig. 5d), and formate (Fig. S10) within the potential range from -0.3 to -0.9 V vs. RHE. CO is not detectable until -0.4 V vs. RHE, and the optimized FE_{CO} is only 78.3 % at -0.6 V vs. RHE. The electrochemical CO_2RR performances of C-Bi-Pd SAA ND catalysts are closely related to the amount of Bi. Doping 3% Bi into Pd (C-Bi_3Pd_{97}-SAA) would not change the main products of C-Pd NDs (CO, H_2 and formate, Figs. 5c–d and S10−11), but it lowers the onset potential of CO formation (−0.3 V vs. RHE) and dramatically suppresses the evolution of H_2 (Fig. 5d), confirming the critical role of Bi in lowering the H coverage on Pd as predicted by DFT calculations. Increasing Bi content to 6% (C-Bi_6Pd_{94}-SAA NDs) leads to apparently reduced $FE_{formate}$ compared to C-Bi_3Pd_{97}-SAA ND catalyst from -0.3 to -0.9 V vs. RHE (Fig. S10), due to the weaker H affiliation of the C-Bi_6Pd_{94}-SAA ND catalyst. The FEs of CO on C-Bi_6Pd_{94}-SAA NDs reach the optimal values of 90.5 % and 91.5 % at -0.4 and -0.5 V vs. RHE (Fig. 5c), respectively, with the corresponding overpotential as low as 290 mV at -0.4 V vs. RHE. [40] These results testify that

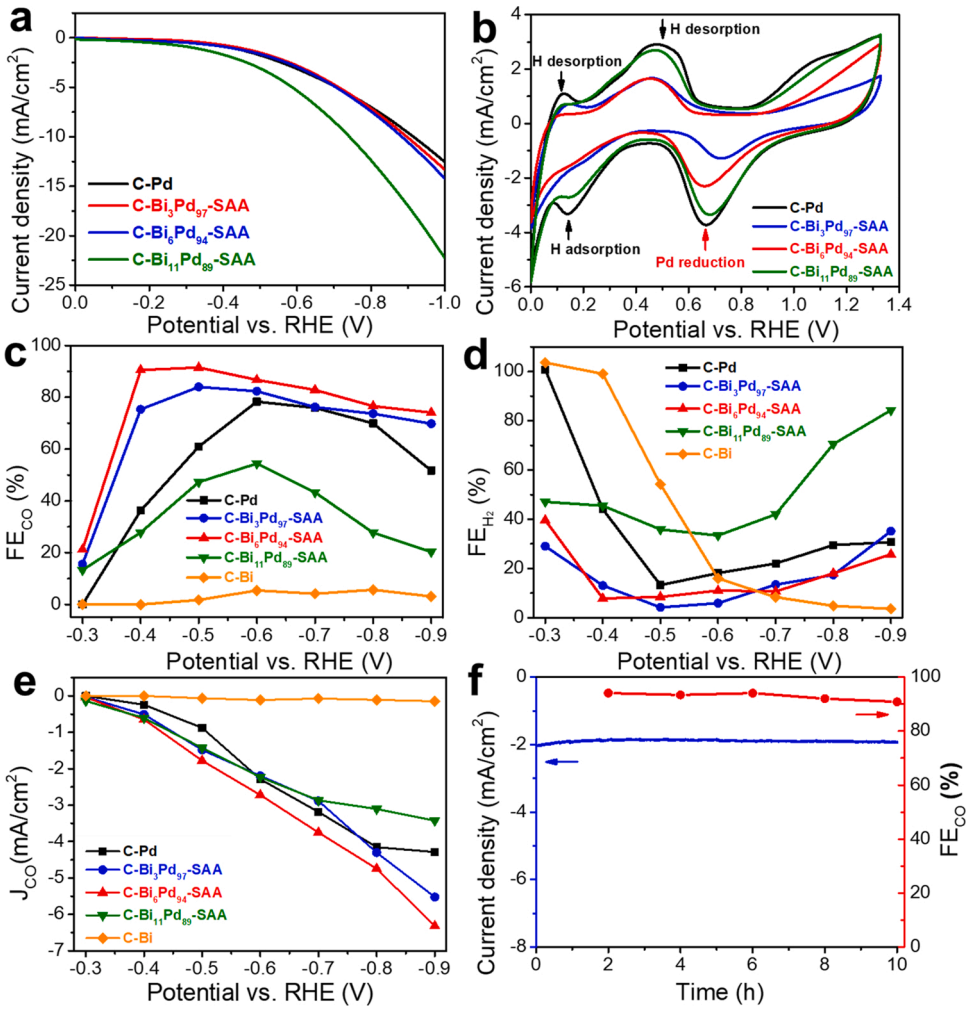

Fig. 5. (a) LSV and (b) CV curves of different catalysts with scan rates of 10 and 50 mV/s, respectively. Reduction potential dependent FEs of (c) CO and (d) H_2 for electrochemical CO_2RR on different catalysts. (e) Geometric area normalized current densities of CO (J_{CO}) on different catalysts. (f) The current density and FE_{CO} of C-Bi_6Pd_{94}-SAA during potentiostatic test at -0.5 V for 10 h.

forming Bi-Pd SAA NDs structures can greatly lower the overpotential for CO formation and inhibit the HER. To the best of our knowledge, this value is the lowest among the reported Pd-based electrocatalysts to reach FE_{CO} more than 90 % in H-type cell (Table S1). Further increasing Bi amount (C-$Bi_{11}Pd_{89}$-SAA NDs) reduces the CO selectivity but favors H_2 or formate (with the highest $FE_{formate}$ of 39.7 % at -0.3 V vs. RHE) formation within the investigated potentials (-0.3 to -0.9 V vs. RHE). It is probably caused by the enrichment of Bi on the surface of $Bi_{11}Pd_{89}$-SAA NDs which alters the surface electronic structure increasing H adsorption and coverage during CO_2RR. For pure C-Bi catalyst, formate is the dominant product with FE reaching 93 % at -0.9 V vs. RHE (Figs. S10 and S11), which is consistent with previous reports [44,45]. As suggested by the DFT calculations (Fig. 1) and CV curves (Fig. 5b), the greatly enhanced selectivity and reduced overpotential of CO formation on the C-Bi_6Pd_{94}-SAA NDs can be attributed to the elevated reaction barrier for HER and hampered formate formation stemming from the weaker H affinity, and the decreased free energy for *COOH formation.

The geometric area normalized partial current density of CO for C-Bi_6Pd_{94}-SAA ND catalyst at -0.4 and -0.5 V vs. RHE in H-type cell are 0.7 and 1.9 mA/cm^2 (Fig. 5e, Fig. S12a), and the corresponding Pd mass normalized current density for CO are 1.8 and 5.0 A/g (Fig. S12b), respectively, which are competitive to the best of the reported Pd-based catalysts in H-type cell (Table S1). Additionally, the C-Bi_6Pd_{94}-SAA NDs maintains high selectivity for CO after 10 h potentiostatic stability test at -0.5 V vs. RHE (Fig. 5f), and its structure and morphology are well preserved after test (Fig. S13 and S14), indicating its robustness for electrochemical CO_2RR.

The *in-situ* XANES and XRD measurements of Pd-based (Pd [29,61], PdAg, PdCu, and PdNi [62]) nanocatalysts indicate that Pd-hydride (PdH_x) is probably formed during electrolysis at certain potentials. The *in-situ* XANES study of Pd NPs for CO_2RR suggest that the metallic Pd surface is the active site for CO formation while the formed Pd-hydride promotes formate production [29]. Besides, the *in-situ* XRD measurements of Pd-based NPs reveal that alloying Pd with certain kinds of elements (Ni, Ag, and Cu) would prominently negatively shift the potential for Pd-hydride formation during CO_2RR [62]. The formation of Pd/Pt core/shell structure is also found to inhibit the formation of Pd-hydride during electrolysis [61]. In this work, no observable peak shift to a lower diffraction degree is measured in the XRD pattern of C-Bi_6Pd_{94}-SAA ND catalyst (Fig. S13) after potentiostatic stability test at -0.5 V for 10 h, suggesting that no significant Pd-hydride formation at optimized potentials (-0.4 to -0.5 V) for CO production, considering that the dissociation of H_2 from Pd-hydride requires high temperature treatment which is usually larger than 100 °C under ambient pressure [63]. The inhibited Pd-hydride formation on Bi_6Pd_{94}-SAA NDs is probably originated from the decreased H affinity due to the introduction of single Bi atoms into Pd lattice.

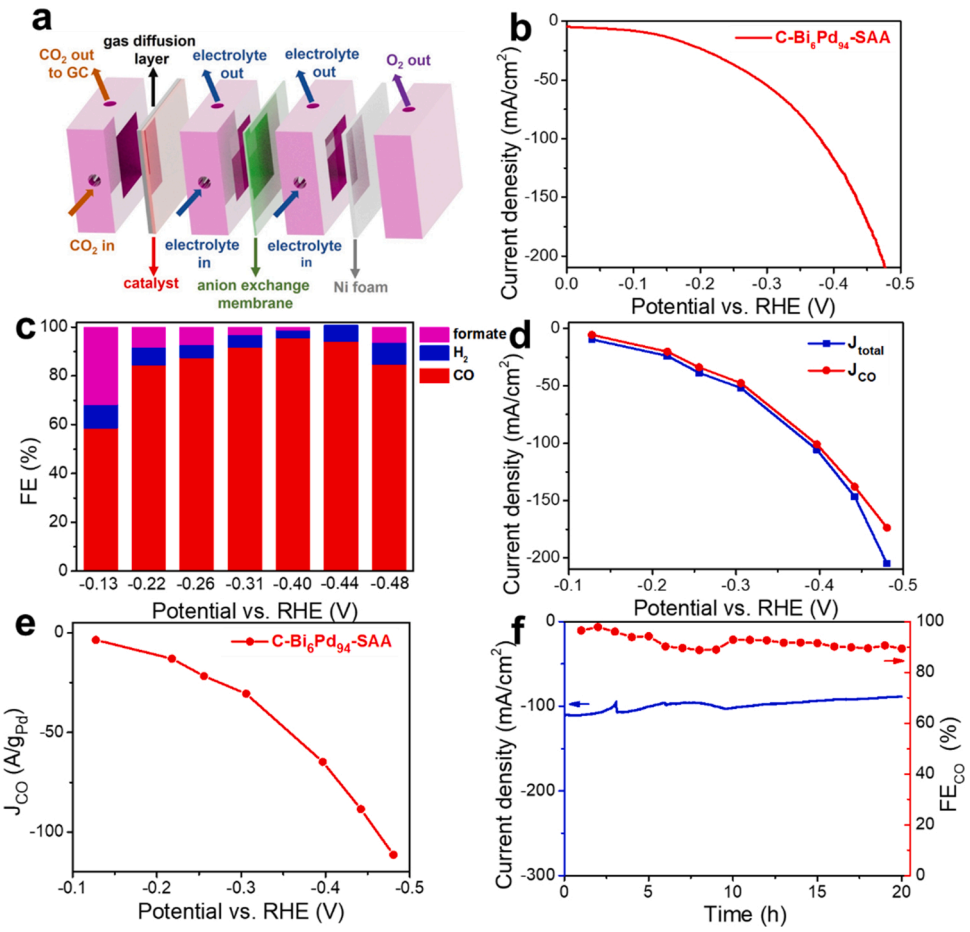

Fig. 6. (a) Illustration of the gas diffusion flow cell for electrochemical CO_2RR. (b) LSV curve of C-Bi_6Pd_{94}-SAA ND catalyst with scan rate of 50 mV/s. (c) FEs of CO, H_2, and formate for electrochemical CO_2RR. (d) Geometric area normalized total (J_{total}) and CO partial (J_{CO}) current densities. (e) Pd mass normalized partial current density of CO (J_{CO}). (f) The current density and FE_{CO} of C-Bi_6Pd_{94}-SAA during potentiostatic test at -0.40 V for 20 h.

3.4. Gas diffusion flow cell tests

The performance of the C-Bi_6Pd_{94}-SAA ND catalyst for electrochemical CO_2RR are further investigated in a gas diffusion flow cell (Fig. 6a). The current densities recorded from the CO_2RR polarization curve on C-Bi_6Pd_{94}-SAA in a gas diffusion flow cell (Fig. 6b) are greatly enhanced compared to that in an H-type cell (Fig. 5a), due to the largely increased CO_2 concentration on catalyst surface. Consequently, the overpotential for CO formation on C-Bi_6Pd_{94}-SAA significantly decreases in a gas diffusion flow cell. CO can be initially detected at -0.13 V vs. RHE with a FE of 58.6 % corresponding to an overpotential of only 20 mV (Fig. 6c), indicating the high activity of C-Bi_6Pd_{94}-SAA for CO formation. The FE_{CO} reaches 91.8 % at -0.31 V vs. RHE with overpotential as low as 200 mV. Additionally, the FEs of CO are all above 90 % within the potential range from -0.31 to -0.44 V vs. RHE, illustrating the excellent selectivity of CO on C-Bi_6Pd_{94}-SAA ND catalyst. The maximum FE_{CO} is 95.8 % at -0.40 V vs. RHE. Further lowering potential leads to the increased H_2 and formate formation at -0.48 V vs. RHE, resulting in the slightly suppressed CO selectivity (FE_{CO} of 84.7 %). The geometric area and Pd mass normalized current densities of CO at -0.44 and -0.48 V vs. RHE are 137.9 and 173.7 mA/cm^2 (Fig. 6d, Table S4), as well as 88.4 and 111.4 A/g_{Pd} (Fig. 6e), respectively, with the corresponding CO production rates of 2.63 and 3.24 mmol/(h·cm^2) (Table S4). Such performance is competitive among the reported catalysts in a gas diffusion flow cell for CO formation at similar potentials (Table S4). Additionally, the large current density and high CO selectivity are well preserved after potentiostatic stability test at -0.40 V vs. RHE for 20 h (Fig. 6f), further testifying the robustness of the C-Bi_6Pd_{94}-SAA ND catalyst for efficient CO formation.

4. Conclusions

In summary, guided by DFT calculations, Bi-Pd SAA ND catalysts are successfully prepared for the first time for the efficient and selective electrochemical CO_2 reduction to CO. XAS characterizations indicate that Bi atoms are atomically dispersed in Pd host. In CO_2RR, the developed Bi-Pd SAA NDs demonstrate Bi content dependent overpotential and FE for CO generation. The best-performing C-Bi_6Pd_{94}-SAA ND catalyst exhibits the FE_{CO} of 90.5 % and 91.8 % at -0.4 and -0.31 V vs. RHE in H-type and gas diffusion flow cells with the overpotentials of only 290 and 200 mV, respectively, which are the lowest among the reported Pd-based electrocatalysts. The maximum geometric area and Pd mass normalized current densities of CO are as high as 173.7 mA/cm^2 and 111.4 A/g_{Pd} at -0.48 vs. RHE in a gas diffusion flow cell, respectively. In addition, the C-Bi_6Pd_{94}-SAA ND catalyst also reveals a robust structure and excellent stability during CO_2RR. The significantly enhanced activity and selectivity for CO formation on the C-Bi_6Pd_{94}-SAA ND catalyst can be attributed to the reduced surface H coverage stemming from the weaker H affinity than pure Pd, which inhibits H_2 and formate formation and decreases the reaction barrier for *COOH generation. Our work highlights an effective strategy for the rational design and synthesis of SAA metal electrocatalysts for efficient electrochemical CO_2RR to value-added products.

CRediT authorship contribution statement

Huan Xie: Conceptualization, Data curation, Writing - original draft. **Yangyang Wan:** Data curation, Writing - original draft. **Xiaoming Wang:** Data curation, Writing - original draft. **Jiashun Liang:** Data curation. **Gang Lu:** Data curation, Writing - original draft, Project administration. **Tanyuan Wang:** Writing - review & editing. **Guoliang Chai:** Writing - review & editing. **Nadia Mohd Adli:** Writing - review & editing. **Cameron Priest:** Writing - review & editing. **Yunhui Huang:** Writing - review & editing. **Gang Wu:** Writing - review & editing. **Qing Li:** Conceptualization, Writing - review & editing, Supervision, Project administration.

Declaration of Competing Interest

The authors report no declarations of interest.

Acknowledgement

This work was financially supported by National Nature Science Foundation of China (21972051) and National Materials Genome Project (2016YFB0700600). The work at California State University Northridge was supported by NSF-PREM program (DMR-1828019). The authors thank the Analytical and Testing Center of Huazhong University of Science and Technology (HUST) for carrying out the ICP-MS, XPS and XRD measurements.

Appendix A. Supplementary data

Supplementary material related to this article can be found, in the online version, at doi:https://doi.org/10.1016/j.apcatb.2020.119783.

References

[1] D.D. Zhu, J.L. Liu, S.Z. Qiao, Adv. Mater. 28 (2016) 3423–3452.
[2] H. Xie, T. Wang, J. Liang, Q. Li, S. Sun, Nano Today 21 (2018) 41–45.
[3] W. Zhu, Y.J. Zhang, H. Zhang, H. Lv, Q. Li, R. Michalsky, A.A. Peterson, S. Sun, J. Am. Chem. Soc. 136 (2014) 16132–16135.
[4] X. Li, W. Bi, M. Chen, Y. Sun, H. Ju, W. Yan, J. Zhu, X. Wu, W. Chu, C. Wu, Y. Xie, J. Am. Chem. Soc. 139 (2017) 14889–14892.
[5] J. Wang, S. Kattel, C.J. Hawxhurst, J.H. Lee, B.M. Tackett, K. Chang, N. Rui, C. J. Liu, J.G. Chen, Angew. Chem. Int. Ed. 58 (2019) 6271–6275.
[6] D. Higgins, C. Hahn, C. Xiang, T.F. Jaramillo, A.Z. Weber, ACS Energy Lett. 4 (2018) 317–324.
[7] T. Möller, W. Ju, A. Bagger, X. Wang, F. Luo, T. Ngo Thanh, A.S. Varela, J. Rossmeisl, P. Strasser, Energy Environ. Sci. 12 (2019) 640–647.
[8] H. Xie, S. Chen, F. Ma, J. Liang, Z. Miao, T. Wang, H.L. Wang, Y. Huang, Q. Li, ACS Appl. Mater. Interfaces 10 (2018) 36996–37004.
[9] D. Kim, J. Resasco, Y. Yu, A.M. Asiri, P. Yang, Nat. Commun. 5 (2014) 4948–4955.
[10] Q. Li, J.J. Fu, W.L. Zhu, Z.Z. Chen, B. Shen, L.H. Wu, Z. Xi, T.Y. Wang, G. Lu, J. J. Zhu, S.H. Sun, J. Am. Chem. Soc. 139 (2017) 4290–4293.
[11] Q. Li, W. Zhu, J. Fu, H. Zhang, G. Wu, S. Sun, Nano Energy 24 (2016) 1–9.
[12] K. Manthiram, B.J. Beberwyck, A.P. Alivisatos, J. Am. Chem. Soc. 136 (2014) 13319–13325.
[13] M. Zhao, Y. Gu, W. Gao, P. Cui, H. Tang, X. Wei, H. Zhu, G. Li, S. Yan, X. Zhang, Z. Zou, Appl. Catal. B: Environ. 266 (2020), 118625.
[14] S. Pérez-Rodríguez, N. Rillo, M.J. Lázaro, E. Pastor, Appl. Catal. B: Environ. 163 (2015) 83–95.
[15] J.-H. Kim, H. Woo, S.-W. Yun, H.-W. Jung, S. Back, Y. Jung, Y.-T. Kim, Appl. Catal. B: Environ. 213 (2017) 211–215.
[16] S.R. Foit, I.C. Vinke, L.G.J. de Haart, R.A. Eichel, Angew. Chem. Int. Ed. 56 (2017) 5402–5411.
[17] S. Guo, S. Zhao, X. Wu, H. Li, Y. Zhou, C. Zhu, N. Yang, X. Jiang, J. Gao, L. Bai, Y. Liu, Y. Lifshitz, S.T. Lee, Z. Kang, Nat. Commun. 8 (2017) 1828–1836.
[18] M.B. Ross, C.T. Dinh, Y. Li, D. Kim, P. De Luna, E.H. Sargent, P. Yang, J. Am. Chem. Soc. 139 (2017) 9359–9363.
[19] W. Sheng, S. Kattel, S. Yao, B. Yan, Z. Liang, C.J. Hawxhurst, Q. Wu, J.G. Chen, Energy Environ. Sci. 10 (2017) 1180–1185.
[20] J. Qiao, Y. Liu, F. Hong, J. Zhang, Chem. Soc. Rev. 43 (2014) 631–675.
[21] H. Tao, X. Sun, S. Back, Z. Han, Q. Zhu, A.W. Robertson, T. Ma, Q. Fan, B. Han, Y. Jung, Z. Sun, Chem. Sci. 9 (2018) 483–487.
[22] W. Zhu, R. Michalsky, O. Metin, H. Lv, S. Guo, C.J. Wright, X. Sun, A.A. Peterson, S. Sun, J. Am. Chem. Soc. 135 (2013) 16833–16836.
[23] Y. Yoon, A.S. Hall, Y. Surendranath, Angew. Chem. Int. Ed. 55 (2016) 15282–15286.
[24] A. Klinkova, P. De Luna, C.-T. Dinh, O. Voznyy, E.M. Larin, E. Kumacheva, E. H. Sargent, ACS Catal. 6 (2016) 8115–8120.
[25] W. Zhu, L. Zhang, P. Yang, C. Hu, Z. Luo, X. Chang, Z.J. Zhao, J. Gong, Angew. Chem. Int. Ed. 57 (2018) 11544–11548.
[26] Y. Li, S. Chen, R. Long, H. Ju, Z. Wang, X. Yu, F. Gao, Z. Cai, C. Wang, Q. Xu, J. Jiang, J. Zhu, L. Song, Y. Xiong, Nano Energy 34 (2017) 306–312.
[27] D. Gao, H. Zhou, F. Cai, J. Wang, G. Wang, X. Bao, ACS Catal. 8 (2018) 1510–1519.
[28] B. Jiang, X.G. Zhang, K. Jiang, D.Y. Wu, W.B. Cai, J. Am. Chem. Soc. 140 (2018) 2880–2889.
[29] D. Gao, H. Zhou, F. Cai, D. Wang, Y. Hu, B. Jiang, W.-B. Cai, X. Chen, R. Si, F. Yang, S. Miao, J. Wang, G. Wang, X. Bao, Nano Res. 6 (2107) (2020) 2181–2191.
[30] W. Zhu, S. Kattel, F. Jiao, J.G. Chen, Adv. Energy Mater. 9 (2019) (2019) 1802840–1802845.
[31] H. Huang, H. Jia, Z. Liu, P. Gao, J. Zhao, Z. Luo, J. Yang, J. Zeng, Angew. Chem. Int. Ed. 56 (2017) 3594–3598.
[32] H. Dong, L. Zhang, P. Yang, X. Chang, W. Zhu, X. Ren, Z.-J. Zhao, J. Gong, Chem. Eng. Sci. 194 (2019) 29–35.
[33] D. Gao, H. Zhou, J. Wang, S. Miao, F. Yang, G. Wang, J. Wang, X. Bao, J. Am. Chem. Soc. 137 (2015) 4288–4291.
[34] Y. Mun, S. Lee, A. Cho, S. Kim, J.W. Han, J. Lee, Appl. Catal. B: Environ. 246 (2019) 82–88.
[35] Z. Yin, D. Gao, S. Yao, B. Zhao, F. Cai, L. Lin, P. Tang, P. Zhai, G. Wang, D. Ma, X. Bao, Nano Energy 27 (2016) 35–43.
[36] M. Valenti, N.P. Prasad, R. Kas, D. Bohra, M. Ma, V. Balasubramanian, L. Chu, S. Gimenez, J. Bisquert, B. Dam, S.W. A, ACS Catal. 9 (2019) 3527–3536.
[37] S. Zhu, Q. Wang, X. Qin, M. Gu, R. Tao, B.P. Lee, L. Zhang, Y. Yao, T. Li, M. Shao, Adv. Energy Mater. 8 (2018) 1802238–1802246.
[38] C. Shan, E.T. Martin, D.G. Peters, J.M. Zaleski, Chem. Mater. 29 (2017) 6030–6043.
[39] J. Jiao, R. Lin, S. Liu, W.C. Cheong, C. Zhang, Z. Chen, Y. Pan, J. Tang, K. Wu, S. F. Hung, H.M. Chen, L. Zheng, Q. Lu, X. Yang, B. Xu, H. Xiao, J. Li, D. Wang, Q. Peng, C. Chen, Y. Li, Nat. Chem. 11 (2019) 222–228.
[40] J. Gu, H. C.-S, L. Bai, H.M. Chen, X. Hu, Science 364 (2019) 1091–1094.
[41] M.-J. Cheng, E.L. Clark, H.H. Pham, A.T. Bell, M. Head-Gordon, ACS Catal. (2016) 7769–7777.
[42] M.T. Darby, R. Réocreux, E.C.H. Sykes, A. Michaelides, M. Stamatakis, ACS Catal. 8 (2018) 5038–5050.
[43] Z. Zhao, G. Lu, J. Phys. Chem. C 123 (2019) 4380–4387.
[44] P. Lu, D. Gao, H. He, Q. Wang, Z. Liu, S. Dipazir, M. Yuan, W. Zu, G. Zhang, Nanoscale 11 (2019) 7805–7812.
[45] N. Han, Y. Wang, H. Yang, J. Deng, J. Wu, Y. Li, Y. Li, Nat. Commun. 9 (2018) 1320–1327.
[46] G. Kresse, J. Furthmuller, Phys. Rev. B 54 (1996) 11169–11186.
[47] G. Kresse, J. Furthmüller, Comp. Mater. Sci. 6 (1996) 15–50.
[48] P.E. Blochl, Phys. Rev. B Condens. Matter 50 (1994) 17953–17979.
[49] K. G, J. D, Phys. Rev. B 59 (1999) 1758–1775.
[50] J.P. Perdew, K. Burke, M. Ernzerhof, Phys. Rev. Lett. 77 (1996) 3865–3868.
[51] B. Hammer, L.B. Hansen, J.K. Nørskov, Phys. Rev. B 59 (1999) 7413–7421.
[52] J.P. Perdew, K. Burke, M. Ernzerhof, Phys. Rev. Lett. 78 (1997), 1396-1396.
[53] S. Grimme, J. Antony, S. Ehrlich, H. Krieg, J. Chem. Phys. 132 (2010) 154104–154122.
[54] K. Mathew, R. Sundararaman, K. Letchworth-Weaver, T. Arias, R.G. Hennig, J. Chem. Phys. 140 (2014) 084106–084113.
[55] J.K. Nørskov, J. Rossmeisl, A. Logadottir, L. Lindqvist, J. Phys. Chem. B 108 (2004) 17886–17892.
[56] J.K. Nørskov, T. Bligaard, A. Logadottir, J.R. Kitchin, J.G. Chen, S. Pandelov, U. Stimming, J. Electrochem. Soc. 152 (2005) J23.
[57] B. Lim, M. Jiang, P.H.C. Camargo, E.C. Cho, J. Tao, X. Lu, Y. Zhu, Y. Xia, Science 324 (2009) 1302–1305.
[58] X. Sun, Q. Zhu, X. Kang, H. Liu, Q. Qian, Z. Zhang, B. Han, Angew. Chem. Int. Ed. 55 (2016) 6771–6775.
[59] C. Mondelli, D. Ferri, J. Grunwaldt, F. Krumeich, S. Mangold, R. Psaro, A. Baiker, J. Catal. 252 (2007) 77–87.
[60] S. Davieroa, L.G.P. Montagnea, G. Mairessea, S. Belinb, V. Brioisb, J. Phys. Chem. Solids (2003) 253–260.
[61] A.M. Wise, P.W. Richardson, S.W.T. Price, G. Chouchelamane, L. Calvillo, P. J. Hendra, M.F. Toney, A.E. Russell, Electrochim. Acta 262 (2018) 27–38.
[62] B.M. Tackett, J.H. Lee, J.G. Chen, Accounts Chem. Res. 53 (2020) 1535–1544.
[63] A. Klinkova, P.V. Cherepanov, I.G. Ryabinkin, M. Ho, M. Ashokkumar, A. F. Izmaylov, D.V. Andreeva, E. Kumacheva, Small 12 (2016) 2450–2458.